INTERNATIONAL JOURNAL FOR NUMERICAL METHODS IN FLUIDS, VOL. 25, 1025–1042 (1997)

FINITE ELEMENT ANALYSIS OF THE DUCT FLOW OF BINGHAM PLASTIC FLUIDS: AN APPLICATION OF THE VARIATIONAL INEQUALITY

YEH WANG*

Department of Chemical Engineering, Tunghai University, Taichung, Taiwan 407, Republic of China

SUMMARY

The duct flow of Bingham plastic fluids is analysed with the variational inequality-based finite element method. The problem of tracking the yield surface is solvable through the regularization technique which can be easily incorporated into the existing finite element code. The existence theorem of this method was established through the theory of variational inequalities. A small positive constant is added to the second shear rate invariant, resulting in an apparent viscosity of finite magnitude in the unyielding plug zone. This makes the minimization of the non-differential variational integral possible. In order to achieve convergence at small regularization parameter, a zero-order continuation is employed. It is also shown that a fine tessellation of the flow domain is necessary for tracking the yield surfaces unambiguously. Two classes of duct flow, namely axial flows in eccentric annuli and in an L-shaped duct, were investigated. In both cases it was easy to show the presence of the mobile plugs around the duct centres from the axial velocity profiles; however, the stagnant plugs at the narrow side in eccentric annuli with large eccentricity and near the apex of right-angled corners in an L-shaped duct could only be identified from the calculation of the distributions of the second shear rate or shear stress invariant. © 1997 John Wiley & Sons, Ltd.

Int. J. Numer. Meth. Fluids, **25**: 1025–1042 (1997)

No. of Figures: 19. No. of Tables: 0. No. of References: 23.

KEY WORDS: Bingham plastic fluid; variational inequality; regularization; finite element analysis

1. INTRODUCTION

Viscoplastic fluids combine the behaviour of rigid solids and non-Newtonian viscous liquids by differentiating between physical regions where these descriptions hold according to criteria based on the level of stress in the material. For low stress values the material will not deform, but beyond some critical value it flows as an inelastic non-Newtonian fluid. The Bingham plastic constitutive equation[1] is the most often used model for a viscoplastic material. Here regions of rigid solid and viscous fluid behaviour are separated in terms of the von Mises yield condition. The von Mises yield criterion is of the form

$$\dot{\boldsymbol{\gamma}} = 0 \quad \text{for } \Pi\tau \leqslant Bn^2, \tag{1}$$

---

* Correspondence to: Y. Wang, Department of Chemical Engineering, Tunghai University, Taichung, Taiwan 407, Republic of China.

Contract grant sponsor: National Science Council of Taiwan, Republic of China; Contract grant number: NSC 86-2216-E-029-001.

CCC 0271–2091/97/091025–18 $17.50 *Received September 1996*

where $\boldsymbol{\tau}$ is the dimensionless deviatoric stress tensor. Its scale is given by $h^*(-\mathrm{d}p^*/\mathrm{d}z^*)$, where h^* is the characteristic dimension of a duct and $\mathrm{d}p^*/\mathrm{d}z^*$ is the imposed pressure gradient. $\Pi\tau$ is the second invariant of a tensor and is defined as $\frac{1}{2}\boldsymbol{\tau}:\boldsymbol{\tau}$. $\dot{\boldsymbol{\gamma}}$ is the dimensionless shear rate tensor. Its scale is given by $h^*(-\mathrm{d}p^*/\mathrm{d}z^*)/\eta_\mathrm{B}$, where η_B is the Bingham plastic viscosity of the viscoplastic fluid. Bn is the Bingham number given as $Y/h^*(-\mathrm{d}p^*/\mathrm{d}z^*)$, where Y is the yield stress. The three-dimensional constitutive equation relating the deviatoric stress and the shear rate tensor is given as[2–4]

$$\boldsymbol{\tau}=\left(\frac{Bn}{(\Pi\dot{\gamma})^{1/2}}+1\right)\dot{\boldsymbol{\gamma}}\quad\text{for }\Pi\tau>Bn^2,\tag{2}$$

$$\dot{\gamma}_{ij}=v_{i,j}+v_{j,i},\tag{3}$$

where $\mathbf{v}$ is the fluid velocity and $\Pi\dot{\gamma}$ is defined as $\frac{1}{2}\dot{\boldsymbol{\gamma}}:\dot{\boldsymbol{\gamma}}$. Equations (1) and (2) define two distinct regions of flow. In the first the invariant $\boldsymbol{\tau}$ is less than the yield value and the fluid flows as a solid plug. In the second the stress invariant exceeds the yield stress and the material flows with a dimensionless non-Newtonian viscosity function η defined as $Bn/(\Pi\dot{\gamma})^{1/2}+1$. The fluid and mobile plug regions are separated by a distinct yield surface.

The composite form of the apparent viscosity points to an important flow characteristic of viscoplastic fluids. As $\dot{\boldsymbol{\gamma}}$ becomes small, the plastic contribution $Bn/(\Pi\dot{\gamma})^{1/2}$ will become important; furthermore as the von Mises yield criterion suggests, $\dot{\boldsymbol{\gamma}}$ vanishes in the plug region and η becomes infinite there. Though the discontinuity in the viscosity curve is essential for characterizing the yield surface, the infinite viscosity causes numerical difficulties in computing the flow field in Bingham plastic fluids as the yield surface is approached. Several methods have been proposed for simulation purposes. One may simply adopt a finite viscosity which is about orders of magnitude greater than the apparent viscosity in the yielded region whenever the apparent viscosity approaches infinity.[5,6] However, the adoption of a cut-off value seems too arbitrary.

Another approach to computing with the Bingham model is due to Beris *et al.*,[7] who treated the yield surface as an unknown boundary. The yield criterion served as an additional constraint which is coupled with the equations of motion for determining the free boundary problem. The pressure and velocity distributions were solved simultaneously with the location of the yield surface. Although this approach enabled the tracking of the yield surface, it introduced the complication that the stress distribution is needed at the *a priori* unknown free boundary. Szabo and Hassager[8] also used the same method to study the visoplastic flow in eccentric annular geometries; however, their analysis was restricted to small eccentricity only.

On the other hand, various modified plastic models were proposed such that the viscosity curve remains continuous and smooth as opposed to the discontinuous curve representing the Bingham model. Thus the formidable task of the tracking of yield surfaces may be avoided by using these models. However, with additional parameters introduced,[9–11] these models usually do not reduce to the exact Bingham model in the limit of $\dot{\boldsymbol{\gamma}}=0$ and the smoothness of the viscosity curve obscures the clear line between yielded and unyielded regions.

A number of authors[12–14] have developed variational principles which hold for the inertialess flow of viscosplastic fluids. Glowinski *et al.*[15] were the first to use variational methods systematically to compute viscoplastic flows by combining variational inequalities with either finite element or finite difference numerical approximations and effective minimization techniques. Two numerical techniques were proposed by these authors.[15] One is the augmented Lagrangian method with which one solves an associated boundary value problem. This method has been applied to viscoplastic flow in sudden contractions and non-circular ducts.[16,17] Unfortunately, the flow filed at the corner regions was not clearly resolved. The other is the regularization method. A small, positive constant, namely the regularization parameter, is added to the shear rate invariant. This eliminates the infinite viscosity in the plug zone and enables the minimization of the variational integral. Bercovier and Engelman[18] studied the cavity flow of Bingham fluids with inertial effects and body forces. Though they employed a regularization parameter of 10^{-14} in a penalty finite element formulation and detected stagnant zones at the corners of a square duct at high yield stress, the shapes of the stagnant regions are quite unusual. Wang[19] applied the regularization method to analyse the complex flow of viscoplastic fluids with shear-rate-dependent viscosity. However, the parameter of 10^{-4} used seemed too large and the resolution of the yield surface was not satisfactory. Walton and Bittleston[20] used the same method to solve the axial flow of Bingham fluids in a narrow eccentric annulus. Bittleston and Hassager[21] calculated the tangential flow field of the same fluids in a concentric annulus. These authors also adopted a somewhat large regularization parameter (10^{-8}) without clear explanation. The duct flow of Bingham fluids near the apex of a corner was also considered by Atkinson and Al-Ali[22] based on the method of singular expansion. However, only the singularity results at the corner regions were given in their study. The global flow field in the entire duct could not be obtained by their method.

Although substantial research has been directed at deriving closed-form solutions for viscoplastic fluids in rectilinear and lubrication flows,[23] the analytical solutions can be obtained only for simple geometries such as a tube or a slit. For viscoplastic fluids flowing through the non-circular ducts, numerical means are necessary for calculating the flow field. In the present study the finite element method is used to solve both the global flow field and the flow field in the corner regions. The problem of tracking the yield surfaces separating the sheared from the unsheared, plug flow region is solvable through the application of the regularization method, which can be incorporated into the existing finite element code easily. The distributions of the invariants of the shear rate and shear stress tensors are also presented. These invariants are relevant to the von Mises yield criterion. Furthermore, it is shown here that the shear rate and shear stress invariants, which are calculated by differentiating the fluid velocity, discriminate the yield surfaces more sharply than the velocity profile in many critical cases. The shapes of the yield surfaces thus found are in some way surprising.

2. MATHEMATICAL FORMULATION AND NUMERICAL PROCEDURES

2.1. *Variational formulation for duct flow of Bingham plastic fluids*

Our approach is to apply finite element numerical procedures. It is based on the use of a minimum variational principle for Bingham plastic fluids first given by Prager:[12]

$$J = \int \tfrac{1}{2}\Pi\dot{\gamma}\,\mathrm{d}\Omega + \int Bn(\Pi\dot{\gamma})^{1/2}\,\mathrm{d}\Omega - \int v_z\,\mathrm{d}\Omega, \tag{4}$$

where v_z is the dimensionless axial velocity whose scale is given by $h^{*2}(-\mathrm{d}p^*/\mathrm{d}z^*)/\eta_\mathrm{B}$. Ω is the dimensionless volume of the flow domain. Equation (4) is non-differentiable owing to the infinite viscosity in the plug region. Duvaut and Lions[14] first developed the corresponding variational inequality and later Glowinski *et al.*[15] demonstrated the feasibility of the regularization technique which makes the minimization of (4) possible by adding a small positive constant to $\Pi\dot{\gamma}$. The axial velocity which minimizes (4) is dependent on the regularization parameter. As the parameter becomes smaller, the axial velocity tends weakly to the unique solution of the corresponding variational inequality

$$\int \dot{\gamma}_{ij}(v_z)\dot{\gamma}_{ij}(u_z - v_z)\,\mathrm{d}\Omega + \int Bn(\Pi\dot{\gamma})^{1/2}(u_z)\,\mathrm{d}\Omega - \int Bn(\Pi\dot{\gamma})^{1/2}(v_z)\,\mathrm{d}\Omega \geqslant \int (u_z - v_z)\,\mathrm{d}\Omega \tag{5}$$

for all test velocity fields $u_z(x, y)$.

2.2. *Finite element implementation*

The finite element method was applied to the flow problem by using an isoparametric element. In each element the co-ordinates and the unknown axial velocity can be written as

$$\begin{pmatrix} x \\ y \\ y_z \end{pmatrix} = \sum_{i=1}^{m} \begin{pmatrix} x_i \\ y_i \\ v_i \end{pmatrix} N_i(r, s), \tag{6}$$

where the curvilinear element in the (x, y)-plane has been mapped onto a square in the (r, s)-plane by the shape functions N_i. Here the points (x_i, y_i) are the nodal positions in the (x, y)-plane, v_i are the unknown nodal velocities and m is the number of nodes in the element. It is easy to show that the variational integral attains its stationary value when the following conditions are satisfied:

$$\partial J/\partial v_1 = \partial J/\partial v_2 = \cdots = \partial J/\partial v_m = 0. \tag{7}$$

We now define the inner product

$$\langle f; g\rangle = \int fg \, \mathrm{d}\Omega. \tag{8}$$

Substituting (6) into (4) and performing the differentiation leads to a set of non-linear equations

$$\langle N_{i,x}; \eta v_{z,x}\rangle + \langle N_{i,y}; \eta v_{z,y}\rangle = \langle N_i; 1\rangle, \tag{9}$$

where a subscript comma represents differentiation. Introducing ε as the regularization parameter, the composite viscosity function η can be written as a function of both $\Pi\dot{\gamma}$ and ε:

$$\eta = \frac{Bn}{(\Pi\dot{\gamma} + \varepsilon)^{1/2}} + 1. \tag{10}$$

Using v_z in (6), the shear rate invariant $\Pi\dot{\gamma}$ can be expressed as

$$\Pi\dot{\gamma} = (\sum N_{i,x} v_i)^2 + (\sum N_{i,y} v_i)^2. \tag{11}$$

Furthermore, substituting for v_z in (9) then gives

$$(\langle N_{i,x}; \eta N_{j,x}\rangle + \langle N_{i,y}; \eta N_{j,y}\rangle) v_j = \langle N_i; 1\rangle. \tag{12}$$

This equation set can be written in the familiar standard matrix form

$$K_{ij} v_j = f_i, \tag{13}$$

where now

$$K_{ij} = \langle N_{i,x}; \eta N_{j,x}\rangle + \langle N_{i,y}; \eta N_{j,y}\rangle, \qquad f_i = \langle N_i; 1\rangle. \tag{14}$$

Note that the banded matrix K is symmetric and the approximation equations produced here are identical with those produced by the Galerkin finite element procedure.

The Newton–Raphson method is used for solving the non-linear system of equations arising from the compositive viscosity function. The tolerance of convergence is fixed at 10^{-6}. We have used both nine-node and six-node Lagrangian elements for efficient tessellation of the flow domain. The 3 × 3 Gaussian quadrature method was used for numerical integration within each element. However, the use of too large a regularization parameter not only yields erroneous solutions but also smooths out the boundary between yielded and unyielded regions such that the location of the yield surface cannot be determined unambiguously. In order to achieve convergence at small parameter, a zero-order continuation was used during simulation. Continuation usually starting from a large parameter of about 10^{-2} could be carried out down to the order of 10^{-20}, at which stage the variational integral ceased to change and the transitions of the slopes in the profiles of the shear rate and shear stress invariants could be clearly shown. No-slip conditions are applied at all solid walls. All the calculations were performed on an Fujitsu supercomputer model vpp300. The CPU time spent for a single iteration was about 2 s for 672 elements with a total of 2665 degrees of freedom.

3. NUMERICAL EXAMPLES

3.1. Axial flow in a concentric annulus

We first consider the plastic flow in a concentric annulus where the eccentricity e is zero. The radius of the inner circle is set to 1·0 and the outer radius is 1·4. Note that the characteristic length of the annulus is the radius of the inner circle. It is well known that the yield surface is also annular for Bingham fluids, with a dimensionless gap twice the magnitude of the Bingham number. Thus the annular flow may serve as a check on the validity of the numerical method. Figure 1 shows the finite element tessellation of the half-annulus. Figure 1(a) shows a coarse mesh lay-out with 160 elements and Figure 1(b) shows a fine mesh lay-out with 672 elements. The influence of the regularization parameter on the variational integral is shown in Figure 2. These are the calculated results from the fine mesh at $Bn = 0{\cdot}1$ and 0·2. The minimization of the variational integral J in (4) can be clearly observed, while the values of J decrease as the regularization parameter ε decreases for both cases. The J-values were calculated with the last term in (4) neglected. It can also be seen that the magnitudes of J reduce to a constant value at small ε at $Bn = 0{\cdot}1$. Moreover, for $Bn = 0{\cdot}2$ the value of J decreases almost monotonically and finally reaches the order of 10^{-16}, which clearly indicates that

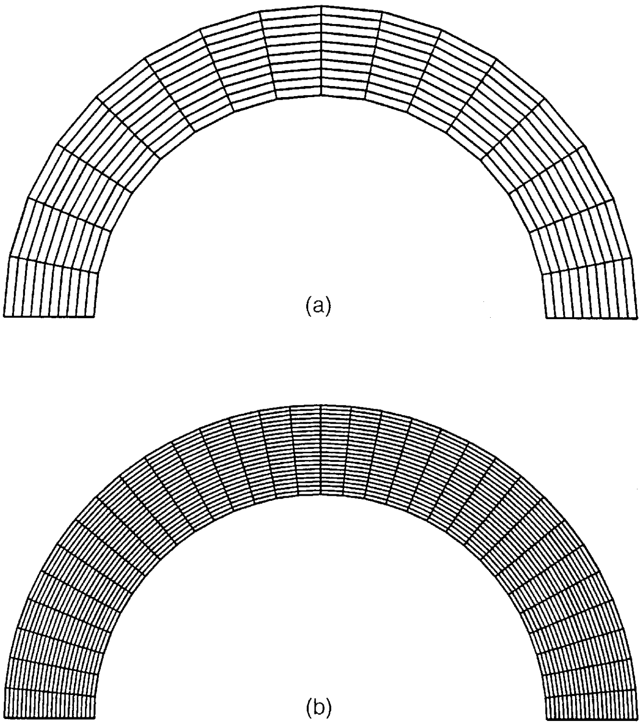

Figure 1. Finite element meshes for calculations in concentric annulus: (a) coarse mesh; (b) fine mesh

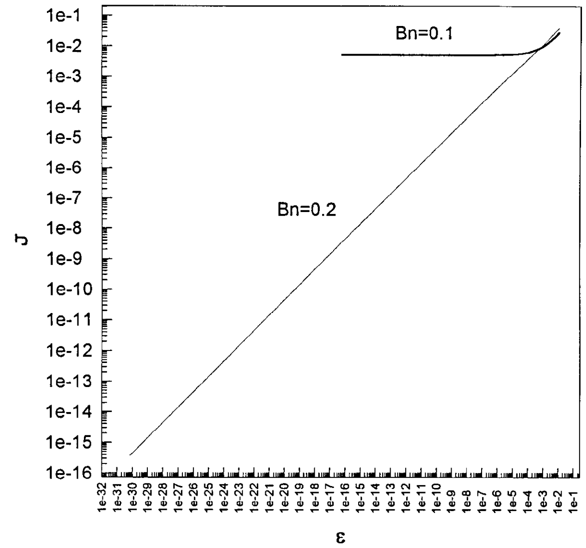

Figure 2. Variation in variational integral J with regularization parameter ε at $Bn=0{\cdot}1$ and $0{\cdot}2$; calculations based on fine mesh

the fluid flow is nearly stagnant in the annulus at $Bn=0{\cdot}2$. Figures 3(a) and 3(b) display the distributions of the axial velocity v_z and the stress invariant $\Pi\tau$ respectively at $Bn=0{\cdot}1$ and $0{\cdot}2$. Full broken lines represent the results at different εs. At $Bn=0{\cdot}1$ calculations were made at $\varepsilon = 10^{-11}$ and 10^{-17} and at $Bn=0{\cdot}2$ calculations were made at $\varepsilon = 10^{-15}$ and 10^{-31}. In order to see the differences in the velocities calculated at $Bn=0{\cdot}2$, a log-scale was used for plotting the velocity profiles. It can be seen that at $Bn=0{\cdot}2$ the plateaux in the velocity profiles nearly fill the gap across the annulus and the magnitudes of v_z are of the order of 10^{-8} and 10^{-16} for $\varepsilon=10^{-15}$ and 10^{-31} respectively. It is apparent that v_z is affected significantly by ε in unyielded regions. Furthermore, the distribution of $\Pi\tau$ is also uniform across the whole gap at $Bn=0{\cdot}2$ for both values of ε. These results clearly indicate that the flow is stagnant at $Bn=0{\cdot}2$. We then examine the calculated results at $Bn=0{\cdot}1$. Both the calculated distributions of v_z and $\Pi\tau$ at $\varepsilon = 10^{-11}$ and 10^{-17} almost coincide, particularly in yielded regions. However, the magnitudes of v_z at the plateaux calculated at different εs can only agree up to

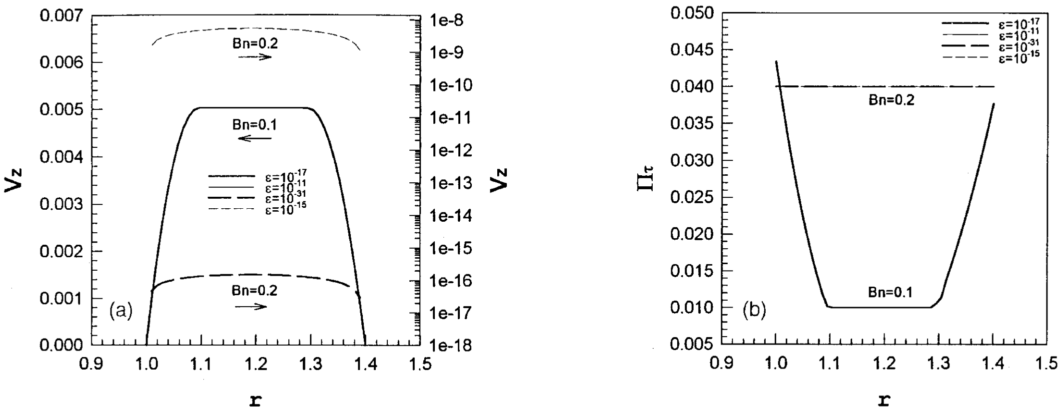

Figure 3. Distributions of (a) axial velocity and (b) stress invariant $\Pi\tau$ along radial direction at various regularization parameters

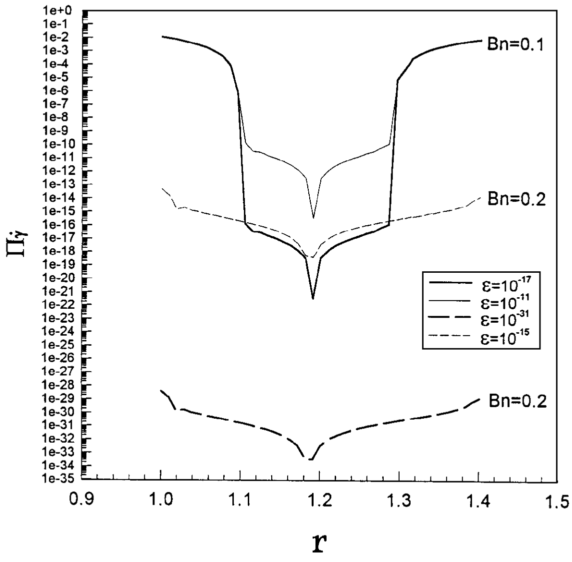

Figure 4. Distributions of shear rate invariant $\Pi\dot{\gamma}$ along radial direction at various regularization parameters

the third significant digit. In addition, plateaux can be seen in both v_z and $\Pi\tau$ curves at $Bn = 0{\cdot}1$ and both plateaux begin at $r = 1{\cdot}1$ and end at $r = 1{\cdot}3$. These plateaux in fact represent the mobile plug region with a width of 0·2. This value agrees exactly with the analytical solution. Also note that at $Bn = 0{\cdot}1$ and 0·2 the plateau values of $\Pi\tau$ are 0·01 and 0·04 respectively, which are just the squares of Bn as dictated by the von Mises yield criterion. Figure 4 displays the distributions of the shear rate invariant $\Pi\dot{\gamma}$ calculated at various εs. It can be seen that there are two branches emanating from the point of minimum $\Pi\dot{\gamma}$ at $Bn = 0{\cdot}1$. In the high-shear-rate region (yielded flow zone) the value of $\Pi\dot{\gamma}$ calculated at both εs are the same, i.e. the value of $\Pi\dot{\gamma}$ in the high-shear-rate region is insensitive to the magnitude of ε. The discontinuity on each branch indicates the location of the yield surface. The left yield surface is at $r = 1{\cdot}1$ and the right at $r = 1{\cdot}3$. However, the discontinuity at $\varepsilon = 10^{-11}$ is more diffuse than that at $\varepsilon = 10^{-17}$. In addition, in the low-shear-rate region (unyielded plug zone) the calculated $\Pi\dot{\gamma}$ at $\varepsilon = 10^{-11}$ is much larger than that at $\varepsilon = 10^{-17}$. In other words, $\Pi\dot{\gamma}$ in the plug zone is also affected enormously by the magnitude of ε. The numerical values can never agree with the exact values owing to the use of the regularization parameter ε. Since we are only interested in the tracking of the yield surface, we shall not pursue the accurate calculation of $\Pi\dot{\gamma}$ in the plug zone further. We next look at the case of $Bn = 0{\cdot}2$. Since the flow is stagnant at $Bn = 0{\cdot}2$, there is only one continuous curve for $\Pi\dot{\gamma}$ across the whole gap of the annulus. Again the calculated $\Pi\dot{\gamma}$ at $\varepsilon = 10^{-15}$ is much larger than that at $\varepsilon = 10^{-31}$. Note that although the velocity profile is able to differentiate the location of the yield surfaces in a concentric annulus, the distributions of $\Pi\dot{\gamma}$ or $\Pi\tau$ are better to use in many critical flow situations, as we shall discuss later.

Figure 5 plots the variational integral J against ε for calculations at $Bn = 0{\cdot}1$ from both fine and coarse meshes, represented by full and broken lines respectively. It can be seen that the two lines almost coincide. The mesh size seems not to affect the value of J significantly. Figures 6(a) and 6(b) display the calculated distributions of the axial velocity v_z and the stress invariant $\Pi\tau$ from coarse and fine meshes respectively at $Bn = 0{\cdot}1$. While the calculated velocity profiles do not exhibit any significant difference, the profiles of the stress invariant clearly show different distributions at the transition from the yielded to the unyielded region, i.e. the yield surface. Figure 7 shows the

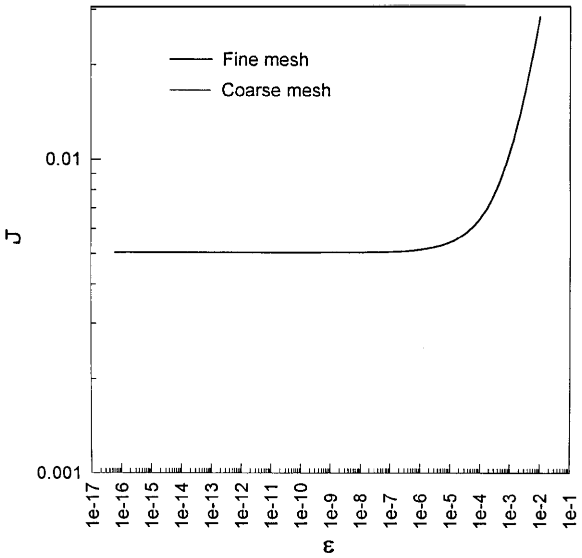

Figure 5. Comparison of variational integral J calculated for two different mesh lay-outs

distributions of the shear rate invariant $\Pi\dot{\gamma}$. Though the discontinuity on the right branch does not differ much, the position of the discontinuity on the left branch for the coarse mesh shows a large deviation from that for the fine mesh. An even finer mesh lay-out was also used, but no significant improvement was found. We therefore decided to use a regularization parameter ε less than 10^{-20} and a fine tesselation with 672 elements in the subsequent computations. We also plot the velocity contours at $Bn = 0{\cdot}1$ and $0{\cdot}15$ in Figures 8(a) and 8(b) respectively. The hatched annular regions in both figures indicate the unyielded plug zones. As expected, the plug zone for $Bn = 0{\cdot}15$ is clearly larger than that for $Bn = 0{\cdot}1$.

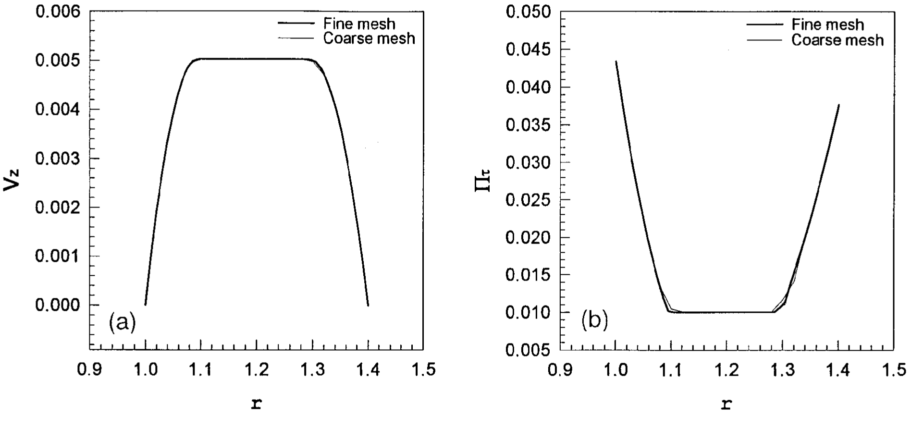

Figure 6. Comparison of (a) axial velocity and (b) stress invariants profiles along radial direction using two different mesh lay-outs

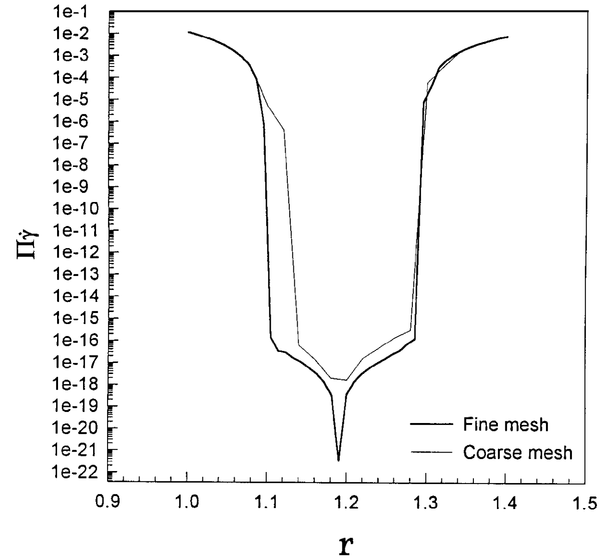

Figure 7. Comparison of shear rate invariant profiles along radial directions using two different mesh lay-outs

3.2. *Axial flow in eccentric annuli*

We then consider an eccentric annulus with an eccentricity e of 0·015. Besides the uniform mesh lay-out consisting of 672 elements, a locally refined mesh around the cap regions of the plug zones consisting of 1092 elements is also used. The uniform mesh and the refined mesh are shown in Figures 9(a) and 9(b) respectively. In the following discussions the results calculated from the uniform mesh and the refined mesh are shown as plus signs and full or broken lines respectively.

The distributions of v_z at the widest gap for Bingham fluids with $Bn=0{\cdot}1$ and 0·15 are shown in Figure 10(a). Since the Newtonian fluid is the limiting case of the Bingham fluid as Bn tends to zero, the results for the Newtonian fluid are also included as a reference. As expected, the Newtonian fluid shows a parabolic distribution of v_z and the Bingham fluids exhibit truncated parabolas. In Figure

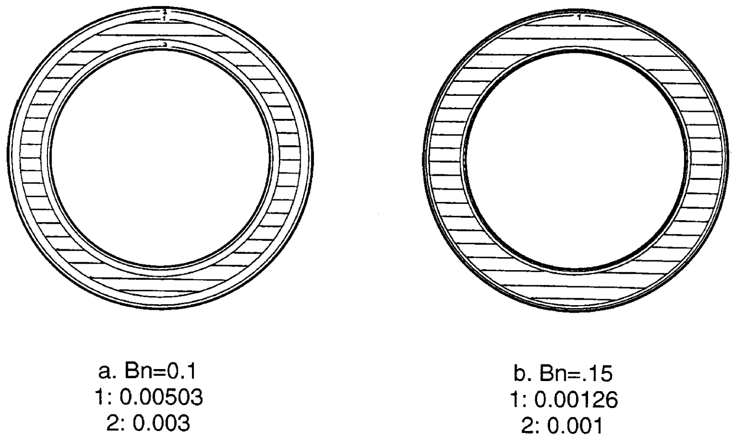

a. Bn=0.1
1: 0.00503
2: 0.003

b. Bn=.15
1: 0.00126
2: 0.001

Figure 8. Velocity contours for Bingham plastic fluids in concentric annulus

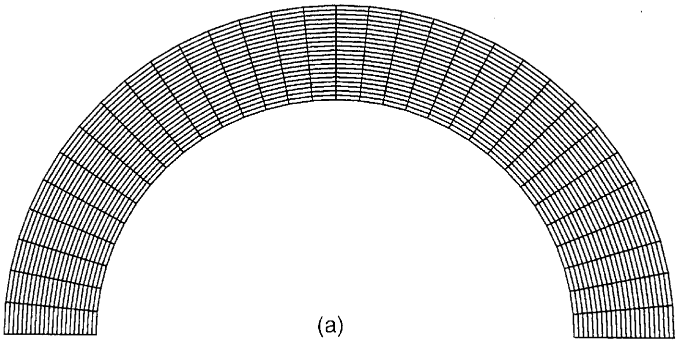

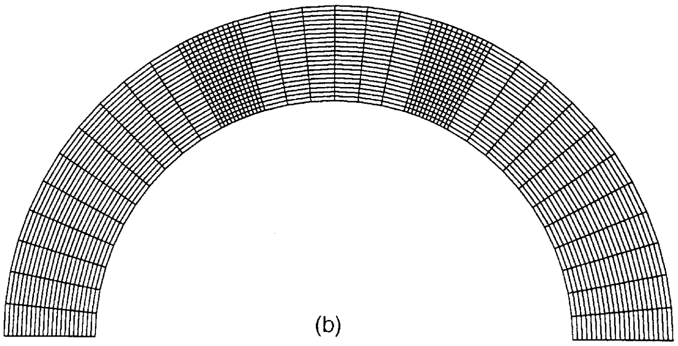

Figure 9. Finite element tessellation of eccentric annulus with $e = 0{\cdot}015$: (a) uniform mesh; (b) locally refined mesh

10(b) the distributions of v_z at the narrowest gap are presented. These distributions again indicate similar profiles to those in Figure 10(a), except that the magnitudes of the velocities are smaller than those in the widest gap. Notice that the width of the plateau at the widest gap (see Figure 10(a)) is larger than that at the narrowest gap (see Figure 10(b)). The azimuthal velocity distributions at the centre of the annulus are shown in Figure 11. The angular position is measured in degrees and is 0° at the widest gap and 180° at the narrowest gap. The Newtonian fluid shows a continuous decrease in

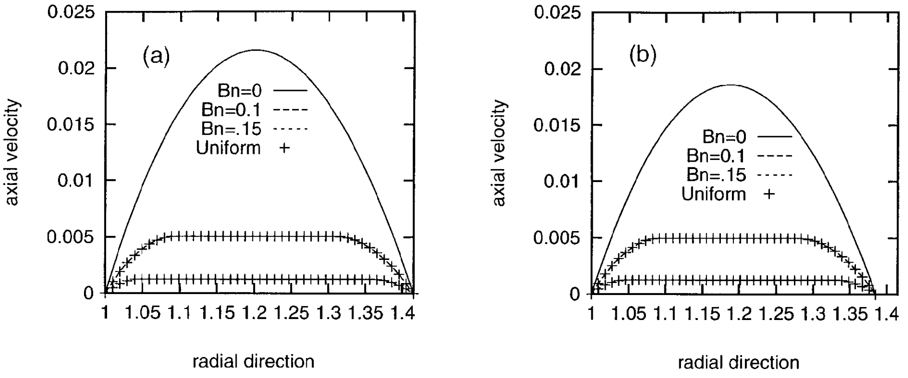

Figure 10. Axial velocity distributions at (a) widest gap and (b) narrowest gap for Bingham fluids in eccentric annulus ($e = 0{\cdot}015$) at various Bingham numbers

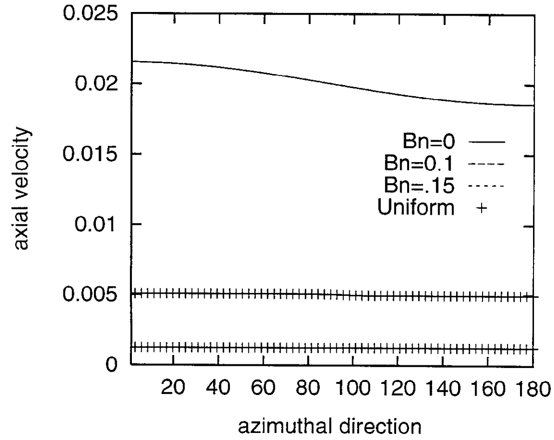

Figure 11. Axial velocity distributions in azimuthal direction for Bingham fluids in eccentric annulus ($e = 0{\cdot}015$ at various Bingham numbers

axial velocity from 0° to 180°. However, no change can be seen for the Bingham fluid with $Bn = 0{\cdot}15$. Furthermore, the velocity distribution for $Bn = 0{\cdot}1$ just barely exhibits two distinct plateaux. The one on the right with larger velocity ($5{\cdot}08 \times 10^{-3}$) corresponds to the plug zone in the widest gap and the one on the left with smaller velocity ($4{\cdot}97 \times 10^{-3}$) corresponds to the plug zone in the narrowest gap. Note that the calculated results for the uniform mesh are almost the same as those for the refined mesh.

In order to see whether these plug zones satisfy the von Mises yield criterion, the azimuthal distributions of $\Pi\tau$ and $\Pi\dot{\gamma}$ are presented in Figures 12(a) and 12(b) respectively. As expected, the $\Pi\tau$s for the Newtonian and Bingham fluids are nearly constant and the magnitudes of $\Pi\tau$ for the Newtonian fluid are the lowest. Note that the magnitude of $\Pi\tau$ for $Bn = 0{\cdot}1$ is slightly larger than the square of Bn; however, $\Pi\tau$ for $Bn = 0{\cdot}15$ is still equivalent to the square of Bn. While the distribution of $\Pi\tau$ does not clearly indicate the existence of the plug zone, the distribution of $\Pi\dot{\gamma}$ seems to show the plug zone more clearly in this case. In Figure 12(b) the profile of $\Pi\dot{\gamma}$ for the Newtonian fluid shows the same shape as $\Pi\tau$, while for the case of $Bn = 0{\cdot}15$, $\Pi\dot{\gamma}$ also remains continuous through the half-annulus with the lowest magnitude. However, the distribution of $\Pi\dot{\gamma}$ for $Bn = 0{\cdot}1$ exhibits two

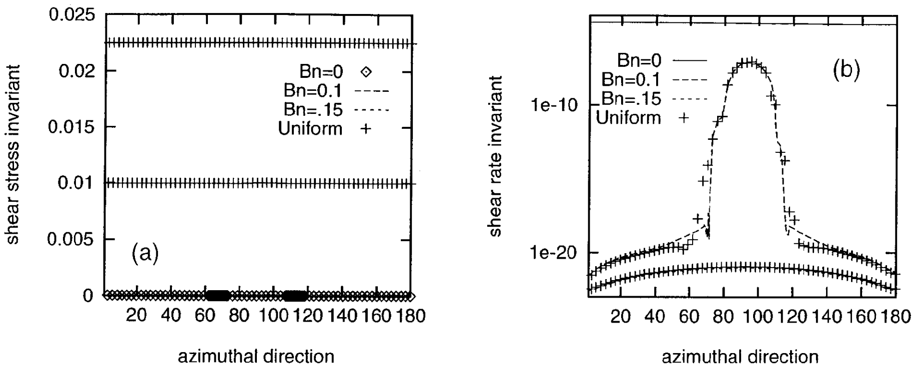

Figure 12. (a) Shear stress and (b) shear rate invariant distributions in azimuthal direction for Bingham fluids in eccentric annulus ($e = 0{\cdot}015$) at various Bingham numbers

distinct step-like jumps at both yield surfaces at about 70° and 118° respectively. When we compare Figure 12(b) with Figure 11, it can be seen that the shear rate invariant, which is discontinuous at the yield surface, discriminates the unyielded plug zone more clearly than the velocity profile. We again note that the calculated results for the uniform mesh almost coincide with those for the refined mesh.

The velocity contours for $Bn=0{\cdot}1$ and $0{\cdot}15$ are shown in Figures 13(a) and 13(b) respectively. The plug zone for $Bn=0{\cdot}1$ is split into two parts because of the development of the azimuthal stress in the eccentric annulus. However, the plug zone for $Bn=0{\cdot}15$ still remains intact because of the high yield stress in the plastic fluid. Some authors[17,20] did not identify the unyielded plug zone at the narrow side of the eccentric annulus. In calculating the velocity field, the latter authors[20] used a relatively large parameter of about 10^{-8} and a relatively coarse tessellation of the flow domain, both of which may lead to poor resolution of the velocity field. The former authors[17] simply ignored the analysis of the velocity field at the narrow side. However, Szabo and Hassager[8] employed the finite element method to simulate the viscoplastic flow in eccentric annular ducts and determined the exact shapes of the two plug zones. Regrettably, their study was restricted to small eccentricity only.

We next take a look at the velocity contours in an eccentric annulus with $e=0{\cdot}2$. Figure 14(a) shows the contours for $Bn=0{\cdot}1$ and Figure 14(b) for $Bn=0{\cdot}15$. The same case has been considered previously.[17,20] The numerical parameters used here are $e=0{\cdot}2$ and $Bn=0{\cdot}15$, which correspond to 0·4 and 0·5 respectively in the aforementioned works. The difference is due to the different scaling. The velocity contour plot and the plug zone at the wide side of the annulus for $Bn=0{\cdot}15$ shown in Figure 14(b) agrees well with the previous results, except that both studies did not identify the exact region of the stagnant plug at the narrow side. Figure 14(a) shows the velocity contour plot for $Bn=0{\cdot}1$. The mobile plug zone at the narrow side nearly fills the gap width. It is worthy of note that for viscoplastic fluids the azimuthal width of the plug zone at the narrow side begins to decrease as the eccentricity increases; however, after the plug zone fills the gap width, the fluid stops flowing inside the plug and the azimuthal width increases as the eccentricity increases. On the other hand, the

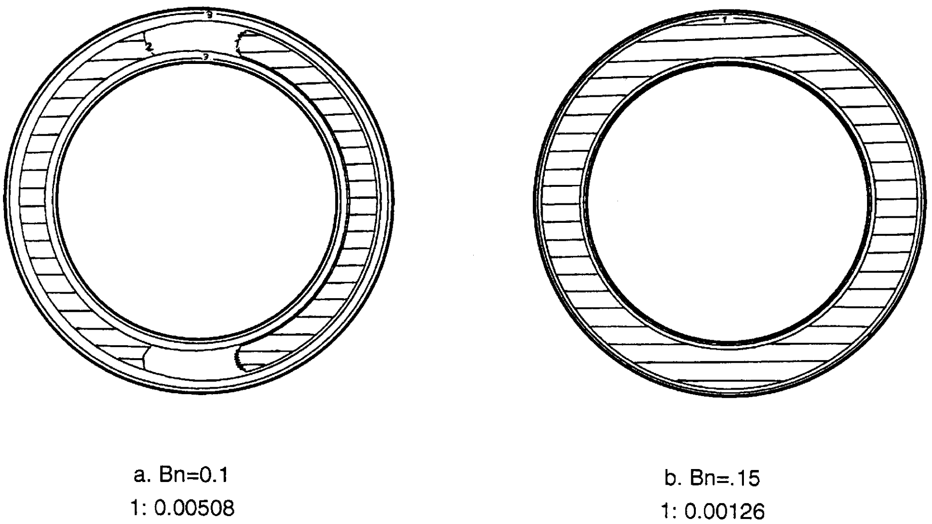

a. Bn=0.1
1: 0.00508
2: 0.00497
3: 0.003

b. Bn=.15
1: 0.00126
2: 0.001

Figure 13. Velocity contours for Bingham plastic fluids in eccentric annulus with $e=0{\cdot}015$

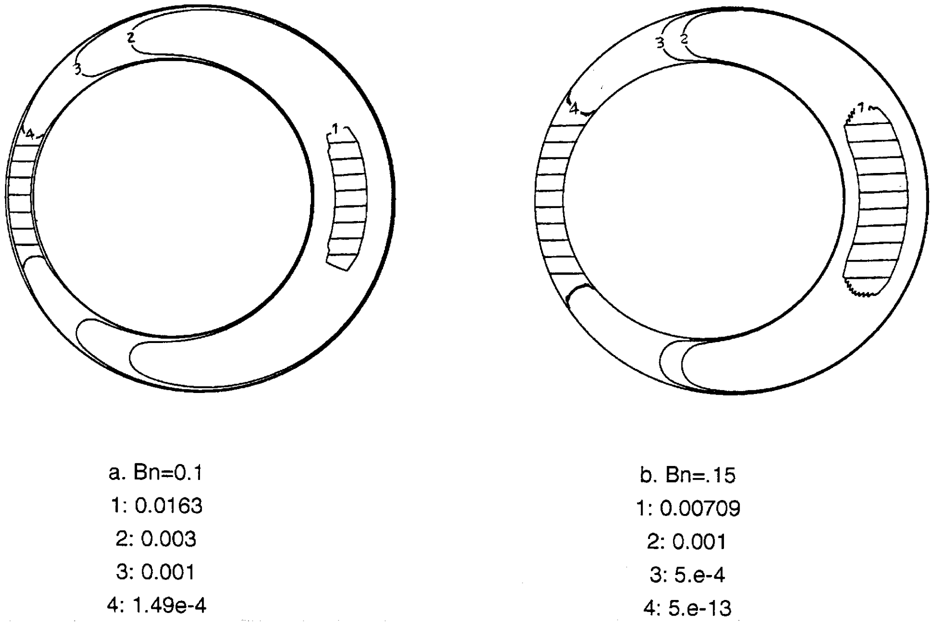

Figure 14. Velocity contours for Bingham plastic fluids in eccentric annulus with $e=0{\cdot}2$

azimuthal width of the plug zone at the wide side keeps decreasing as the eccentricity increases, until the flow becomes stagnant throughout the annulus.

3.3. Axial flow in an L-shaped duct

We also consider the plastic flow in an L-shaped duct. The interest in studying the L-shaped duct lies in the corner singularity which has been reported previously by Atkinson and El-Ali.[22] However, their method of analysis can only calculate the flow field near the apex of the corner and is not applicable to the global flow field in the duct. Huigol and Panizza[17] also analysed the L-shaped duct flow but did not show the exact shape of the stagnant plugs near the right-angled corners.

The finite element mesh for tessellating the flow domain is shown in Figure 15. Figure 15(a) shows a uniform mesh consisting of 2187 elements. Figure 15(b) shows a locally refined mesh around the centre and along all sides, where the number of elements is 1612. The refined mesh was generated relative to a central point at which the axial velocity of the Newtonian fluid is the maximum. Note that the elements surrounding the central point are triangular elements. The shorter sides of the duct are half the lengths of the longer sides. The origin set at the bottom left corner, which is also labelled as the first corner. Other corners are labelled as the second, the third, etc. following the counter-clockwise direction. Note that the fourth corner is the only corner with an included angle of 90°.

The diagonal distributions of the axial velocity starting at the first corner and ending at the fourth corner for the Newtonian fluid and Bingham fluids with $Bn=0{\cdot}1$, $0{\cdot}15$ and $0{\cdot}18$ are shown in Figure 16. The diagonal positions are measured from the first corner to the fourth corner. The results calculated from the refined mesh are shown as the chain line. It can be seen that the axial velocity starts to increase from the first corner in the Newtonian flow, reaches the maximum at the duct centre, then decreases monotonically to the fourth corner. Apparently there are two positions of zero shear. One of them is located at the first corner and the other at the duct centre. Since the Newtonian fluid is

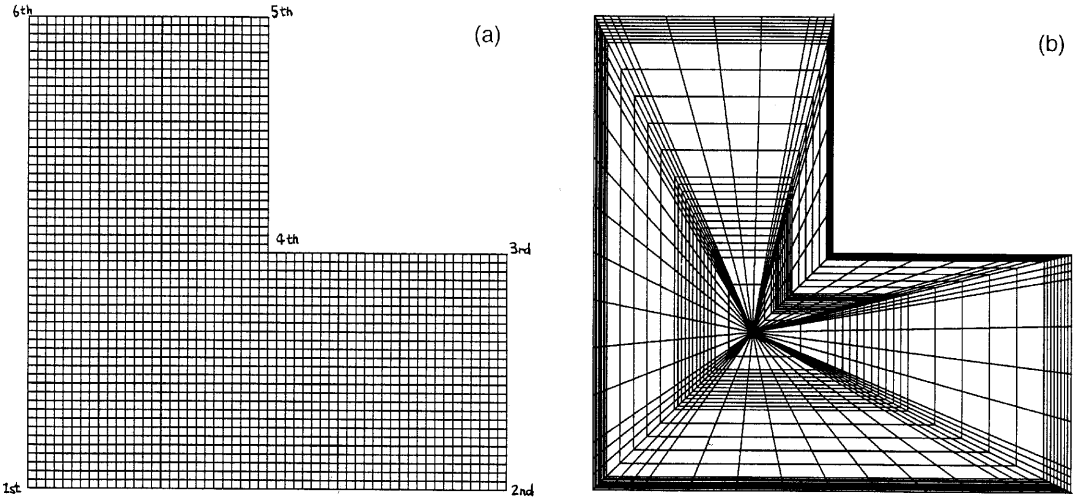

Figure 15. Finite element tesselation of L-shaped duct: (a) uniform mesh; (b) locally refined mesh

the limiting case of the Bingham fluid as *Bn* tends to zero, it is expected to observe two plateaux in Figure 16 for all Bingham numbers. Firstly, the plateaux around the duct centre can be clearly seen, indicating the existence of mobile plugs. These plateaux are in the regions between about 0·31 and 0·61 for $Bn = 0{\cdot}1$, between about 0·24 and 0·66 for $Bn = 0{\cdot}15$ and between about 0·13 and 0·70 for $Bn = 0{\cdot}18$. Secondly, the velocity profiles of Bingham fluids seem to become flat around the first corner, where the magnitudes of the velocity are extremely small. Such results may indicate the existence of stagnant plugs at the first corner. However, it is not easy to see the sizes of these plugs. Also note that the calculated results from the two mesh lay-outs are nearly the same.

The distributions of $\Pi\dot{\gamma}$ calculated from the different mesh lay-outs are presented in Figure 17. Though the results agree well in the high-shear-rate regions, they differ somewhat in the unyielded regions, particularly around the duct centre. None the less, they all display similar profiles. As discussed previously, there are two minima located at the centre and at the first corner in the

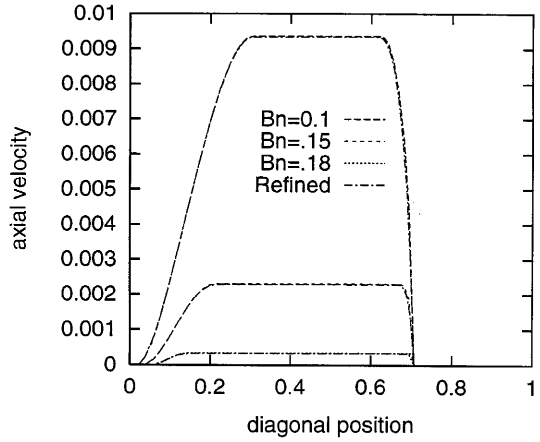

Figure 16. Axial velocity distributions from first corner to fourth corner at various Bingham numbers

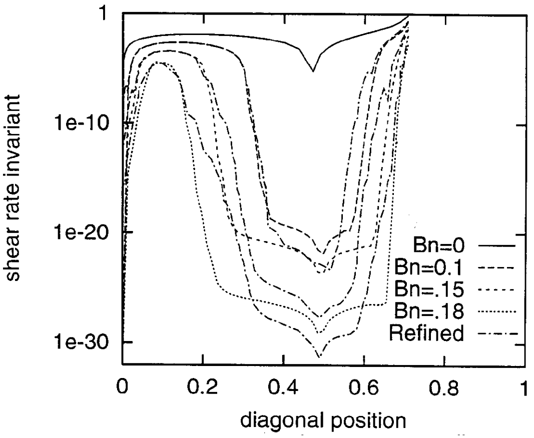

Figure 17. Shear rate invariant distributions from first corner to fourth corner at various Bingham numbers

Newtonian flow. Likewise, distinct changes in slope can be observed in Figure 17 for all Bingham numbers around the duct centre and at the apex of the first corner. The two transitions around the duct centre clearly indicate the regions of the mobile plugs. Though one can see the third transition at the first corner, it is not easy to identify the sizes of the stagnant zones. These plug regions are in general agreement with those shown in the velocity distributions. However, unlike the cases of eccentric annular flow, the distributions of $\Pi\dot{\gamma}$ do not discriminate the yield surfaces very well, particularly around the corner. It is also interesting to note that the $\Pi\dot{\gamma}$ distributions calculated from the uniform mesh show sharper transitions than those calculated from the locally refined mesh. In order to further clarify the positions of the yield surfaces, we are going to look at the distributions of the stress invariant $\Pi\tau$.

In Figure 18 we present the distributions of $\Pi\tau$ calculated from the different mesh lay-outs. Like the velocity distributions, all the calculated $\Pi\tau$s from the different mesh lay-outs are nearly the same. Two flat segments, where the values of $\Pi\tau$ are equal to the squares of *Bn*, can be clearly seen in this plot for all Bingham numbers. The long segments in the middle of the curve correspond to the mobile plugs around the duct centre, while the short segments at the left correspond to the stagnant plugs at

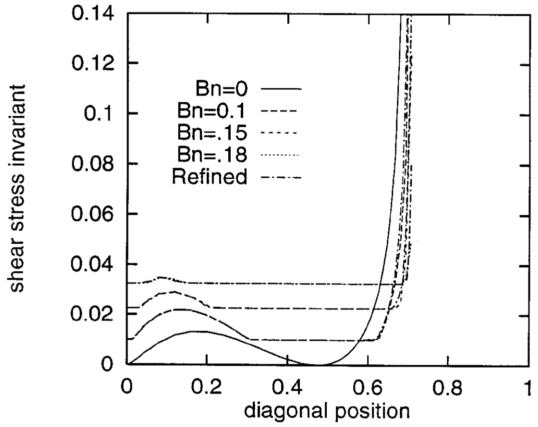

Figure 18. Shear stress invariant distributions from first corner to fourth corner at various Bingham numbers

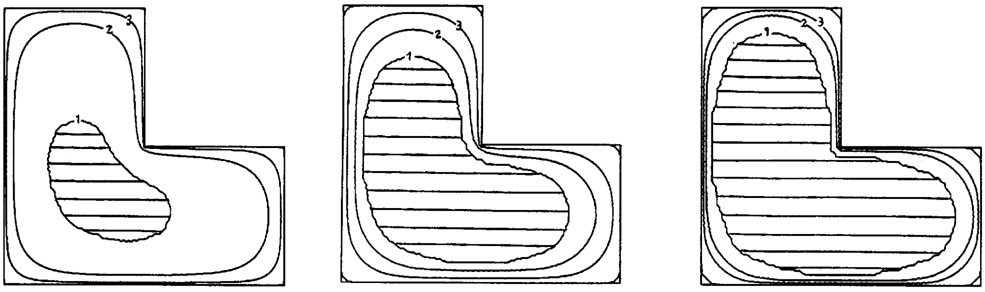

a. Bn=0.1
1: 0.0093729
2: 0.004
3: 0.001
4: 3.e-7

b. Bn=.15
1: 0.0022991
2: 0.002
3: 0.001
4: 2.e-7

c. Bn=.18
1: 3.4007e-4
2: 3.e-4
3: 1.5e-4
4: 2.e-8

Figure 19. Velocity contours for Bingham plastic fluids in L-shaped duct

the first corner. It is interesting to see the enlargement of both the mobile plugs and the stagnant plugs with increasing Bingham number. Furthermore, the breadth of the peak area, which represents the size of the yielded zones, decreases as the Bingham number increases. In fact, the flow will be stagnant everywhere in the duct when the peak disappears. The velocity contour plots for $Bn = 0{\cdot}1$, $0{\cdot}15$ and $0{\cdot}18$ are shown in Figures 19(a)–19(c) respectively. The velocities of both the mobile plugs and the stagnant plugs are decided according to the positions where the flat segments in the distributions of $\Pi\tau$ are found. It can be clearly seen that there are stagnant plugs at all right-angled corners for $Bn = 0{\cdot}15$ and $0{\cdot}18$. However, the size of the stagnant plugs is too small to be seen clearly at $Bn = 0{\cdot}1$.

4. CONCLUSIONS

We have illustrated the use of the finite element method in conjunction with the regularization technique for simulating a pair of steady duct flow problems. Unlike previous studies using the perturbation or singular expansion methods, which were limited to either small annular gap or small eccentricity in eccentric annuli and also limited to corner regions in non-circular ducts, the present technique is applicable to any regions in irregular geometries. Moreover, the effects of the regularization parameter and the refinement of the mesh size on the calculated flow field are analysed in detail. A small regularization parameter and a resonably fine tesselation of the flow domain are necessary for accurate computations. The use of too large a parameter or too coarse a tesselation often leads to poor resolution in critical regions.

For the eccentric annular flow of viscoplastic fluids it has been shown that at small eccentricities there is only a single mobile plug across the whole annulus. Further increase in the eccentricity results in the splitting of the mobile plug and eventually a stagnant zone will appear at the narrow side of the annulus when the eccentricity becomes large enough. For the flow in an L-shaped duct it can be seen clearly that stagnant regions exist at the right-angled corners and no plug zone can be found at the blunt angle of 270°. The size of either the mobile plug or the stagnant plug increases with increasing *Bn*. Also note that as *Bn* tends to zero, the Newtonian fluid is the limiting case of the Bingham fluid. Hence the position of zero shear in a Newtonian flow is also the position of the plug zone in a viscoplastic flow.

In the future it is expected that the present numerical procedure could be extended to two- and three-dimensional flow problems without difficulty. Other viscoplastic models involving shear-rate-dependent viscosities could be included as well.

ACKNOWLEDGEMENT

Partial support of this research by the National Science Council of Taiwan, Republic of China through grant NSC 86-2216-E-029-001 is gratefully acknowledged.

APPENDIX: NOMENCLATURE

Bn	Bingham number, $Y/h^*(-\mathrm{d}p^*\mathrm{d}z^*)$
e	eccentricity (dimensionless)
h^*	characteristic length of duct (dimensional): inner radius for annular flow; length of long side for L-shaped duct flow
J	variational integral given in (4) (dimensionless)
N_i	element shape functions
p^*	fluid pressure (dimensional)
u_z	test fluid velocity (dimensionless)
v_z	axial fluid velocity (dimensionless)
Y	yield stress (dimensional)
x, y	rectangular co-ordinates (dimensionless)
z	axial flow direction (dimensionless)

Greek letters

$\dot{\boldsymbol{\gamma}}$	shear rate tensor
ε	regularization parameter
η	apparent viscosity (dimensionless)
η_{B}	Bingham plastic viscosity (dimensional)
$\Pi\dot{\gamma}$	second invariant of shear rate tensor (dimensionless)
$\Pi\tau$	second invariant of shear stress tensor (dimensionless)
$\boldsymbol{\tau}$	shear stress tensor
Ω	volume of flow domain

REFERENCES

1. E. C. Bingham, *Fluidity and Plasticity*, McGraw-Hill, New York, 1922.
2. K. Hohenemser and W. Prager, 'On the construction of mechanics of isotropic continua', *ZAMM*, **12**, 216–226 (1932).
3. J. G. Oldroyd, 'A rational formulation of the equations of plastic flow for a Bingham solid', *Proc. Camb. Philos. Soc.*, **43**, 100–105 (1947).
4. J. L. White, 'A plastic–viscoelastic constitutive equation to represent the rheological behaviour of concentrated suspensions of small particles in polymer melts', *J. Non-Newtonian Fluid Mech.*, **5**, 177–190 (1979).
5. O. C. Zienkiewicz and P. N. Godbole, 'Viscous, incompressible flow with special reference to non-Newtonian (plastic) fluids', in R. H. Gallagher, J. T. Oden, C. Taylor and O. C. Zienkiewicz (eds), *Finite Elements in Fluids*, Vol. 1, Wiley, New York, 1975, pp. 25–55.
6. O. C. Zienkiewicz, E. Onate and J. C. Heinrich, 'A general formulation for coupled thermal flow of metals using finite elements', *Int. j. numer. methods eng.*, **17**, 1497–1514 (1981).
7. A. N. Beris, J. A. Tsamopoulos, R. C. Armstrong and R. A. Brown, 'Creeping motion of a sphere through a Bingham plastic', *J. Fluid Mech.*, **158**, 219–244 (1985).
8. P. Szabo and O. Hassager, 'Flow of viscoplastic fluids in eccentric annular geometries', *J. Non-Newtonian Fluid Mech.*, **45**, 149–169 (1992).

9. D. K. Gartling and N. Phan-Thien, ‘A numerical simulation of a plastic fluid in a parallel plate plastometer’, *J. Non-Newtonian Fluid Mech.*, **14**, 347–360 (1984).
10. E. J. O’Donovan and R. I. Tanner, ‘Numerical study of the Bingham squeeze film problem’, *J. Non-Newtonian Fluid Mech.*, **15**, 75–83 (1984).
11. T. C. Papanastasiou, ‘Flows of materials with yield’, *J. Rheol.*, **31**, 385–404 (1987).
12. W. Prager, ‘On slow viscoplastic flow’, in *Studies in Mathematics and Mechanics*, Academic, New York, 1954, pp. 208–216.
13. N. Yoshioka and K. Adachi, ‘On variational principles for a non-Newtonian fluid’, *J. Chem. Eng. Jp.*, **4**, 217–220 (1971).
14. G. Duvaut and J. L. Lions, *Inequalities in Mechanics and Physics*, Springer, Berlin, 1976.
15. R. Glowinski, J. L. Lions and R. Tremolires, *Numerical Analysis of Variational Inequalities*, North-Holland, Amsterdam, 1981.
16. P. A. Tanguy, A. Fortin and F. Bertrand, ‘On the imposition of friction boundary conditions for the numerical simulation of Bingham fluid flows’, *Comput. Methods Appl. Mech. Eng.*, **88**, 97–109 (1991).
17. R. R. Huigol and M. P. Panizza, ‘On the determination of the plug flow region in Bingham fluids through the application of variational inequalities’, *J. Non-Newtonian Fluid Mech.*, **58**, 207–217 (1995).
18. M. Bercovier and M. Engelman, ‘A finite element method for the incompressible non-Newtonian flows’, *J. Comput. Phys.*, **36**, 313–326 (1980).
19. Y. Wang, ‘Extrusion of rubber compounds and highly filled thermoplastics through coathanger dies’, *Int. Polym. Proc.*, **6**, 311–317 (1991).
20. I. C. Walton and S. H. Bittleston, ‘The axial flow of Bingham plastic in a narrow eccentric annulus’, *J. Fluid Mech.*, **222**, 39–60 (1991).
21. S. H. Bittleston and O. Hassager, ‘Flow of viscoplastic fluids in a rotating concentric annulus’, *J. Non-Newtonian Fluid Mech.*, **42**, 19–36 (1992).
22. C. Atkinson and K. El-Ali, ‘Some boundary value problems for the Bingham model’, *J. Non-Newtonian Fluid Mech.*, **41**, 339–363 (1992).
23. R. B. Bird, G. C. Dai and B. J. Yarusso, ‘The rheology and flow of viscoplastic materials’, *Rev. Chem. Eng.*, **1**, 1–70 (1983).